

RESEARCH ARTICLE

10.1002/2016JD026436

Key Points:

- The first attempt to assimilate GOES imager radiance data using rapid refresh system with hybrid-3DnVar scheme
- Evaluated the impact of assimilating GOES imager radiance with the rapid refresh assimilation system for convection-permitting forecast over Mexico and obtained some significant positive impact

Correspondence to:

Z. Liu,
liuz@ucar.edu

Citation:

Yang, C., Z. Liu, F. Gao, P. P. Childs, and J. Min (2017), Impact of assimilating GOES imager clear-sky radiance with a rapid refresh assimilation system for convection-permitting forecast over Mexico, *J. Geophys. Res. Atmos.*, *122*, 5472–5490, doi:10.1002/2016JD026436.

Received 29 DEC 2016

Accepted 2 MAY 2017

Accepted article online 5 MAY 2017

Published online 30 MAY 2017

Impact of assimilating GOES imager clear-sky radiance with a rapid refresh assimilation system for convection-permitting forecast over Mexico

Chun Yang¹ , Zhiqian Liu² , Feng Gao³ , Peter P. Childs³, and Jinzhong Min¹

¹Key Laboratory of Meteorological Disaster of Ministry of Education (KLME)/Joint International Research Laboratory of Climate and Environment Change (ILCEC)/Collaborative Innovation Center on Forecast and Evaluation of Meteorological Disaster, Nanjing University of Information Science and Technology, Nanjing, China, ²National Center for Atmospheric Research, Boulder, Colorado, USA, ³Panasonic Avionics Corporation/Panasonic Weather Solution, Morrisville, North Carolina, USA

Abstract The Geostationary Operational Environmental Satellite (GOES) imager data could provide a continuous image of the evolutionary pattern of severe weather phenomena with its high spatial and temporal resolution. The capability to assimilate the GOES imager radiances has been developed within the Weather Research and Forecasting model's data assimilation system. Compared to the benchmark experiment with no GOES imager data, the impact of assimilating GOES imager radiances on the analysis and forecast of convective process over Mexico in 7–10 March 2016 was assessed through analysis/forecast cycling experiments using rapid refresh assimilation system with hybrid-3DnVar scheme. With GOES imager radiance assimilation, better analyses were obtained in terms of the humidity, temperature, and simulated water vapor channel brightness temperature distribution. Positive forecast impacts from assimilating GOES imager radiance were seen when verified against the Tropospheric Airborne Meteorological Data Reporting observation, GOES imager observation, and Mexico station precipitation data.

1. Introduction

Nowadays, satellite data assimilation has become an indispensable part in numerical weather prediction (NWP) system. It provides 90–95% of the actively assimilated data [Bauer *et al.*, 2010]. As the development of fast radiative transfer models and their adjoint models, a number of clear-sky or all-sky infrared and microwave channel radiance observations from satellite instruments have been assimilated directly into most operational centers, such as the National Centers for Environmental Prediction (NCEP), European Centre for Medium-Range Weather Forecasts (ECMWF), Met Office, Japan Meteorological Agency, Météo-France, and Environment Canada [Greenwald *et al.*, 2002; Heilliette and Garand, 2007; Pavelin *et al.*, 2008; McNally, 2009; Pangaud *et al.*, 2009; Heilliette, 2010; Bauer *et al.*, 2010; Geer *et al.*, 2010; Geer and Bauer, 2010; Guidard *et al.*, 2011; Lupu and McNally, 2012; Okamoto, 2013; Zhu *et al.*, 2013; Kazumori, 2014; Yang *et al.*, 2016]. These infrared and microwave instruments are carried on different geostationary and polar-orbiting satellites.

The main focus in recent years is on polar-orbiting satellites carrying sounding instruments such as the advanced microwave sounding unit (AMSU), the Atmospheric Infrared Sounder, or the Infrared Atmospheric Sounding Interferometer [Liu *et al.*, 2012; McNally *et al.*, 2006; Xu *et al.*, 2013]. Assimilation of radiance observation from polar-orbiting satellites can offer significant benefit, especially in data-sparse areas, like the Tropics or the Southern Hemisphere. That is because they have higher data resolution than ground-based measurements and provide global coverage, which is necessary for NWP model.

The geostationary instruments, such as the Meteosat Visible and Infrared Imager (MVIS), the Spinning Enhanced Visible and Infrared Imager (SEVIRI), and the Geostationary Operational Environmental Satellite (GOES) imagers, have lower spectral resolution, which leads to less capability in terms of vertical sounding for the atmosphere than polar-orbiting instruments [Stengel *et al.*, 2009]. Despite their low spectral resolution, geostationary instruments provide a nearly continuous image of the evolutionary pattern of weather phenomena at mesoscale to the convective scale in the observed domain due to their high spatial and temporal resolutions [Montmerle *et al.*, 2007; Stengel *et al.*, 2009; Zou *et al.*, 2011].

Many studies have been made to directly and indirectly assimilate observations from geostationary satellite into global or regional NWP system in recent years. For instance, in global system, *Köpken et al.* [2004] assimilated MVIRI on board Meteosat-7 with 4D-Var system at ECMWF, *Szyndel et al.* [2005] assimilated SEVIRI on board Meteosat-8 with 4D-Var system, and *Su et al.* [2003] assimilated GOES imager observations in the NCEP Global Data Assimilation System. In these studies at global scale, the main result showed small improvement in the analysis and the forecast skill. *Montmerle et al.* [2007] and *Stengel et al.* [2009] investigated the impact of SEVIRI at regional scale in the Aldin/France model 3D-Var system and High Resolution Limited Area Model 4D-Var system, respectively. The results showed that SEVIRI radiances have a positive impact on the very short-range forecast. *Chen et al.* [2015, 2016] developed the observation operator for cloud liquid water path and cloud ice water path and assimilated these retrieved cloud products from GOES with 3D-Var. It showed that assimilating GOES cloud products has improved the accuracy of temperature, humidity, and wind analysis. *Zou et al.* [2011], *Qin et al.* [2013], and *Zou et al.* [2015] employed NCEP Gridpoint Statistical Interpolation 3D-Var scheme to assimilate GOES imager, which led to significant improvement of the quantitative precipitation forecast near the coast of Gulf of Mexico and the track and intensity forecast of Hurricane Debby (2012).

The above studies were all based on variational methods, including 3D-Var and 4D-Var. In this paper, we investigate impacts of GOES imager radiance data with “hybrid-3D-EnVar” assimilation method [*Wang et al.*, 2008a, 2008b; *Schwartz et al.*, 2015] and the rapid refresh assimilation system. Many previous studies have proved that the hybrid method can bring great benefit for initializing NWP model forecasts by incorporating flow-dependent background error covariances (BECs) within a variational framework [*Wang et al.*, 2008b, 2013; *Schwartz and Liu*, 2014; *Xu et al.*, 2015]. In addition, GOES is a geostationary satellite and scanning the Earth with 15 min interval. By using the rapid refresh assimilation system, GOES imager data can be assimilated with hourly cycling to catch the evolution of mesoscale systems.

In this study, as the first attempt to assimilate GOES imager radiance in the Weather Research and Forecasting (WRF) model’s data assimilation (WRFDA) system [*Barker et al.*, 2012], the impact of assimilation GOES imager radiance will be evaluated for convection-permitting analyses and forecasts over Mexico. The rest of this paper is organized as follows. Section 2 describes the WRFDA hybrid system and GOES imager observation. The method of blending, calibration, zenith angle calculation, quality control, and bias correction will be discussed in section 3, while section 4 details the experimental configurations. Results are shown in section 5 with conclusions presented in section 6.

2. Model and Observation

2.1. The WRFDA Dual-Resolution Hybrid-3D-EnVar Algorithm

As described in *Wang et al.* [2008a], the hybrid-3D-EnVar (refer to as “hybrid” hereafter) algorithm in WRFDA system incorporates ensemble background error (BE) into a variational cost function using the extended control variable approach [*Lorenc*, 2003]. The cost function J with analysis increment can be defined as

$$J(\mathbf{x}'_1, \mathbf{a}) = \beta_1 \frac{1}{2} (\mathbf{x}'_1)^T \mathbf{B}^{-1} (\mathbf{x}'_1) + \beta_2 \frac{1}{2} \mathbf{a}^T \mathbf{A}^{-1} \mathbf{a} + \frac{1}{2} (\mathbf{y}' - \mathbf{H}\mathbf{x}')^T \mathbf{R}^{-1} (\mathbf{y}' - \mathbf{H}\mathbf{x}'). \quad (1)$$

The first term of the right hand is the traditional 3D-Var background term with the static \mathbf{B} . \mathbf{x}'_1 is the increment associated with the 3D-Var static BECs. The last term is the observation term with observation error covariance \mathbf{R} and linearized observation operator \mathbf{H} , where \mathbf{y}' is the observation increment and \mathbf{x}' is the analysis increment of the hybrid. In the second term, \mathbf{A} is a block diagonal matrix that constrains the extended control vector \mathbf{a} , performing the localization of the ensemble covariance. The two factors β_1 and β_2 are the weights placed on the static background error covariance and the ensemble covariance. They are constrained by

$$\frac{1}{\beta_1} + \frac{1}{\beta_2} = 1. \quad (2)$$

The vertical localization of ensemble covariance at model level k is realized by a Gaussian correlation function defined as

$$C(k, k_1) = \exp\left(-\frac{(k_1 - k)^2}{(10k/N)^2}\right), \quad (3)$$

where k_1 is the model level index and N the number of model levels.

Table 1. GOES-13 Imager Channel Center Frequency and Data Resolution

Channel Number	Center Frequency (μm)	Data Resolution (km)
1	0.65	1.0
2	3.9	4.0
3	6.5	4.0
4	10.7	4.0
6	13.3	8.0

In this study, we use “dual resolution” hybrid analysis, which can combine a high-resolution background with a low-resolution ensemble to produce a high-resolution analysis, with no need for high-resolution ensemble. For dual-resolution hybrid, the ensemble is at lower resolution than the background.

Therefore, it has fewer extended control variables than single-resolution hybrid analyses and can save I/O, computational cost, and memory use [Schwartz *et al.*, 2015].

2.2. GOES Imager Data

The GOES satellites are operated by the United States National Oceanic and Atmospheric Administration (NOAA) National Environmental Satellites, Data, and Information Service. The first GOES satellite was launched on 16 October 1975. The current NOAA operational geostationary satellites are GOES-13 and GOES-15. Both of them are positioned at an altitude of 35,800 km above the equator. They provide the imager data over the East Coast (GOES-13) and West Coast (GOES-15) from 75°W and 135°W in geostationary orbits. Due to the coverage limitation, in this paper, we estimate the impact of GOES imager data assimilation over Mexico with GOES-13 observation.

As shown in Table 1, GOES-13 imager has five channels: one visible channel with its central wavelength located at 0.65 μm (channel 1) and four infrared channels 2, 3, 4, and 6, whose central wavelengths are located at 3.9, 6.5, 10.7, and 13.3 μm , respectively. The spatial resolution of channel 1 is 1 km at the subsatellite point, and channels 2, 3, and 4 are 4 km, while channel 6 is 8 km.

Different channels of GOES-13 have different purposes. Visible channel 1 is for observing the reflected solar radiation from the Earth. It can be used for detecting clouds, aerosols, and surface feature during daytime. Channel 2 is a shortwave infrared channel, which provides the midinfrared radiation for analyzing cloud patterns and terrestrial features. Channel 3 is a water vapor channel for depicting midlevel and upper level water vapor and clouds. Channel 4 and channel 6 are longwave infrared channels. Channel 4, the window channel, can provide surface skin or cloud top temperature except for thin cirrus. The 12 μm channel 5 on GOES-8 through 11 was replaced by 13.3 μm channel 6 on GOES-13. With 13.3 μm central wavelength, channel 6 is mainly used for cloud detection.

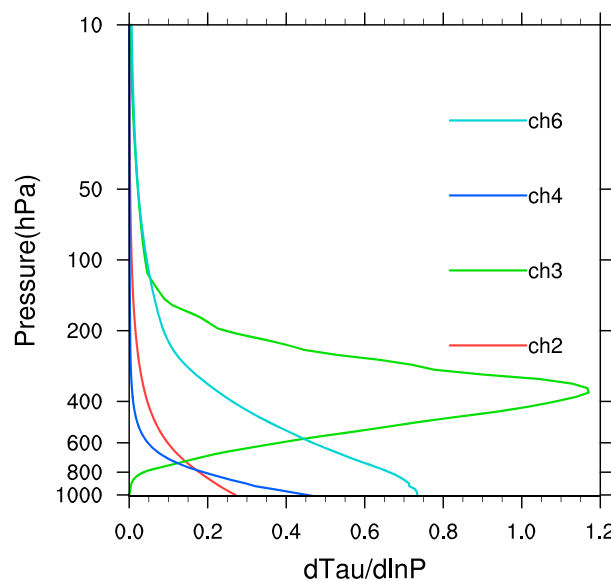


Figure 1. Weighting functions (unitless) of GOES imager channel 2 to channel 6 at 3.9 (red), 6.5 (green), 10.7 (blue), and 13.3 μm (cyan), calculated using CRTM based on the U.S. standard atmosphere.

Calculated from the U.S. Standard Atmosphere using the Community Radiative Transfer Model (CRTM) [Weng, 2007], weighting functions of GOES-13 imager channel 2 to channel 6 with four wavelengths are shown in Figure 1. Water vapor channel 3’s weighting function peaks on average around 400 hPa. Channel 6 is located near the carbon dioxide absorption band and provides information on the low-level temperature, so it peaks on average 900 hPa. Channel 2 and channel 4 are more transparent to clear-sky atmosphere with contribution weight peaking at lowest level.

3. Methodology

3.1. The Calibration of GOES Imager Data

The GOES imager radiance data used in this study are downloaded from the

Table 2. GOES-13 Scaling Coefficients

Channel	m	b
2	227.3889	68.2167
3	38.8383	29.1287
4	5.2285	15.6854
6	5.5297	16.5892

Comprehensive Large Array-Data Stewardship System of NOAA (https://www.class.ngdc.noaa.gov/saa/products/search?datatype_family=GVAR_IMG).

There are a few formats to choose from, such as image formats (GIF and JPG), Network Common Data Form (NetCDF), Area and Raw. The NetCDF data are

used in this study. Latitude and longitude can be read from NetCDF files, but the raw satellite data in these files are not brightness temperature but GOES Variable (GVAR) counts. Therefore, the GVAR count data in NetCDF files must first be converted to radiance or brightness temperature before assimilation.

The steps of calibration built in WRFDA are shown as follows [Weinreb and Han, 2011]: (1) converting the 16 bit data to 10 bit data (0–1023) by dividing 32 and (2) converting imager GVAR count to scene radiance.

$$R = (X - b)/m, \tag{4}$$

where R is radiance and X is the GVAR count value. The coefficients m and b are the scaling slope and intercept, respectively, and are listed in Table 2.

1. Converting imager radiance to effective temperature

$$T_{\text{eff}} = \frac{c_2 * v}{\ln[1 + (c_1 * v^3)/R]}, \tag{5}$$

where T_{eff} is effective temperature and R is radiance. v , c_1 , and c_2 are the central wave number of the channel and the two radiation constants, respectively.

$$\begin{aligned} c_1 &= 1.191066 \times 10^{-5}, \\ c_2 &= 1.43833 \end{aligned} \tag{6}$$

2. Converting effective temperature to actual temperature

$$T = \alpha + \beta * T_{\text{eff}} + \lambda * T_{\text{eff}}^2, \tag{7}$$

where α , β , and γ are three conversion coefficients. These three coefficients and central wave number v of channel 2 to channel 6 used in this study are listed in Table 3.

3.2. Calculation of Satellite Zenith Angle

The satellite zenith angle, which is a CRTM input parameter for radiance assimilation, can be calculated by latitude, longitude, and its position in geostationary orbit. GOES-13 is located at 75°W, so $\text{lon}_{\text{sat}} = -75 * \pi/180$.

$$\theta = |\text{lon} - \text{lon}_{\text{sat}}|, \tag{8}$$

$$\begin{aligned} r_1 &= (2 * r_e * \sin(\theta/2) - r_e * (1 - \cos(\text{lat})) * \sin(\theta/2))^2, \\ &+ (2 * r_e * (\text{lat}/2))^2 - (r_e * (1 - \cos(\text{lat})) * \sin(\theta/2))^2 \end{aligned} \tag{9}$$

$$\theta_1 = 2 * \sin^{-1}((2 * \sin^{-1}(\sqrt{r_1})/r_e/2), \tag{10}$$

$$\theta_2 = \tan^{-1}(r_e * \sin\theta_1 / (r_h + r_e * (1 - \sin\theta_1))), \tag{11}$$

$$\theta_z = (\theta_1 + \theta_2) * 180/\pi, \tag{12}$$

where θ_z is satellite zenith angle, r_e is Earth radius, r_h is the altitude of geostationary satellite in orbit, and lat and lon are the latitude and longitude of each pixel in radians.

3.3. Quality Control

The quality control procedure is applied to GOES imager radiances, including (1) removing pixels with mixed surface types; (2) channels 2, 4, and 6 data over land are discarded, and only water pixels are assimilated; (3) rejecting pixels with $\text{CLWP} \geq 0.2 \text{ kg/m}^2$, which is calculated from background; (4) data are

Table 3. GOES-13 Imager Coefficients

Channel	ν	α	β	γ
2	2561.7421	-1.4755462	1.0028656	-5.8203946e-07
3	1522.5182	-4.1556932	1.0142082	-8.0255086e-06
4	937.23449	-0.52227011	1.0023802	-2.0798856e-06
6	749.82589	-0.16089410	1.0006896	-3.9853774e-07

removed for the difference between channel 4 simulated value and observations larger than the thresholds, which is 3.5 K over land and 2.5 K over ocean [Hocking et al., 2010], for cloud detection; (5) the observations are not used if the absolute value of bias-corrected innovation exceeds 15; and (6) departure check, which removes the observations if the bias-corrected innovation exceeded $3\sigma_o$, where σ_o is the observation error standard deviation.

3.4. Bias Correction and Observation Error Statistic

The same bias correction method, variational bias correction (VarBC) [Dee, 2004], described in Yang et al. [2016] is used for GOES imager data to correct the systematic error before they are assimilated. The cost function J to be minimized with respect to the bias parameters and model state becomes

$$J(\mathbf{x}', \mathbf{a}, \boldsymbol{\beta}') = \beta_1 \frac{1}{2} (\mathbf{x}')^T \mathbf{B}^{-1} (\mathbf{x}') + \beta_2 \frac{1}{2} \mathbf{a}^T \mathbf{A}^{-1} \mathbf{a} + \frac{1}{2} (\boldsymbol{\beta}')^T \mathbf{B}_\beta^{-1} (\boldsymbol{\beta}') + \frac{1}{2} [\mathbf{y} - \tilde{H}(\mathbf{x}', \boldsymbol{\beta}')]^T \mathbf{R}^{-1} [\mathbf{y} - \tilde{H}(\mathbf{x}', \boldsymbol{\beta}')], \tag{13}$$

where $\boldsymbol{\beta}'$ is the increment of bias correction coefficient vector and \mathbf{B}_β is the bias parameter background error covariance, respectively [Auligné et al., 2007]. \tilde{H} is the modified forward operator, which combines the radiative transfer model and a linear combination of a set of predictors. In this study, four predictors are chosen to correct the bias, including 1000–300 and 200–50 hPa layer thicknesses, surface skin temperature, and total column water vapor.

The bias correction coefficients are updated adaptively during the analysis cycling using the bias coefficients from the previous cycle’s analysis as the background. The initial implementation is the statistic from 48 times GOES observations with VarBC off-line scheme [Liu et al., 2012].

The observation error statistic is generated with 48 times GOES observations after quality control and listed in Table 4.

4. Experimental Setup

Before 7 March 2016, an upper low moved across southern California, United States, and produced thunderstorms (not shown here). The powerful subtropical jet stream generated a progressively deeper trough (Figure 2), forming a slow-moving closed low. This system was developing and moving southeastward into Mexico. As shown in Figure 2d below, from 1200 UTC 7 March to 0000 UTC 9 March, an upper low was formed and featured a large 552 Dm height contour. Such a large, strong upper low appears to be an unprecedented event in modern weather observations for Mexico. In the low level (850 hPa; Figure 3), with the southerly flow, more moisture was delivered from ocean to the west and southwest coast of Mexico. In United States, because of the heavy moisture transport from Gulf of Mexico, many locations experienced extreme rainfall and flash flooding, particularly across East Texas and North Louisiana, United States. In this study, the main focus is the Mexico area.

The 500 hPa heights and the 850 hPa water vapor show a textbook heavy rainfall pattern. With the developing trough on the eighth and ninth, there was heavy precipitation into the southwest coast and the Mexico City (Figure 4). The upper level low also brought the cold air to the north of Mexico.

Table 4. The Observation Error for GOES-13 Imager Channels 2, 3, 4, and 6

Channel	2	3	4	6
Obs error (K)	1.75	1.32	0.77	0.72

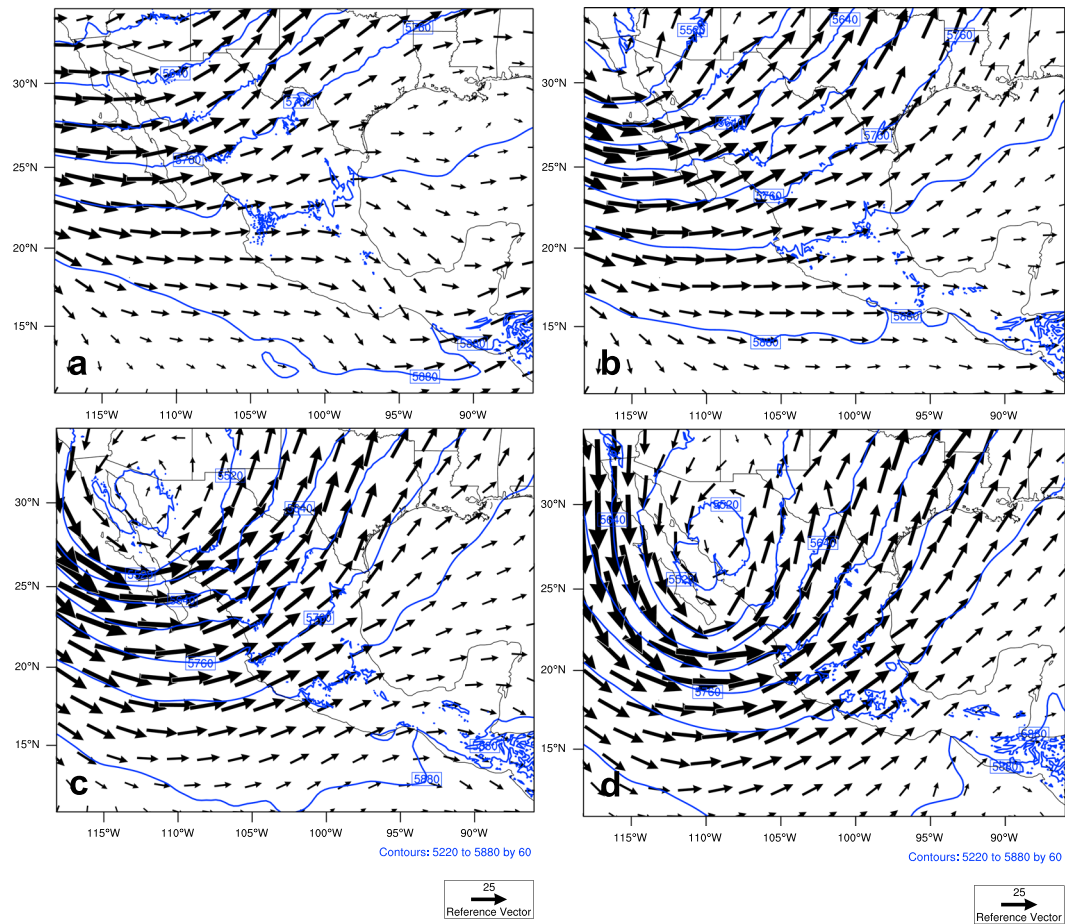


Figure 2. 500 hPa height (m) and wind vector (m/s) in (a) 1200 UTC 7 March 2016, (b) 00 UTC 8 March, (c) 12 UTC 8 March, and (d) 00 UTC 9 March.

For evaluating the assimilation of GOES imager radiances with this system, we performed hourly cycling forecast-analysis experiments for the period from 0000 UTC 7 March 2016 to 0000 UTC 9 March 2016, and four 24 h forecasts are initialized from 1200 UTC 7 March, 0000 UTC 8 March, 1200 UTC 8 March, and 0000 UTC 9 March analyses with the rapid refresh assimilation system. In order to match Mexico precipitation station observation time, an additional 24 h precipitation forecast is made from 1400 UTC 8 March to 1400 UTC 9 March.

All experiments employ version 3.7 of the Advanced Research WRF Model (hereafter WRF [Skamarock et al., 2008]). Two nested domains are configured with a parent domain of 12 km horizontal resolution with 400 * 300 model grid points and an inner two-way nesting domain at 4 km with 898 * 721 grid points (Figure 5). Both the parent domain and inner domain have 51 vertical levels with the model top at 50 hPa. The following physics parameterizations are used: WRF Morrison 2-moment scheme [Morrison, et al., 2009]; the Rapid Radiative Transfer Model for GCM [Mlawer et al., 1997; Iacono et al., 2008] shortwave and longwave radiation schemes; the Yonsei University boundary layer scheme [Hong et al., 2006]; the Monin-Obukhov surface layer scheme [Monin and Obukhov, 1954]; the unified Noah land-surface mode [Chen and Dudhia, 2001]; and the Kain-Fritsch cumulus parameterization scheme [Kain, 2004].

In the cycling experiments, analyses are generated every hour. The lateral boundary conditions for 1 h and 24 h forecasts are provided by the NCEP Global Forecast System (GFS) forecasts. The backgrounds for the following cycles are always the previous cycle's 1 h forecast blended with the global GFS forecast. The 12 km deterministic and ensemble fields for each hour are produced from the 80 ensemble numbers of GFS T574 global ensemble forecast. For the inner domain, 4 km ensembles are not needed. The ensemble background error for 4 km dual-resolution hybrid analysis is provided by 12 km prior ensemble. Thus,

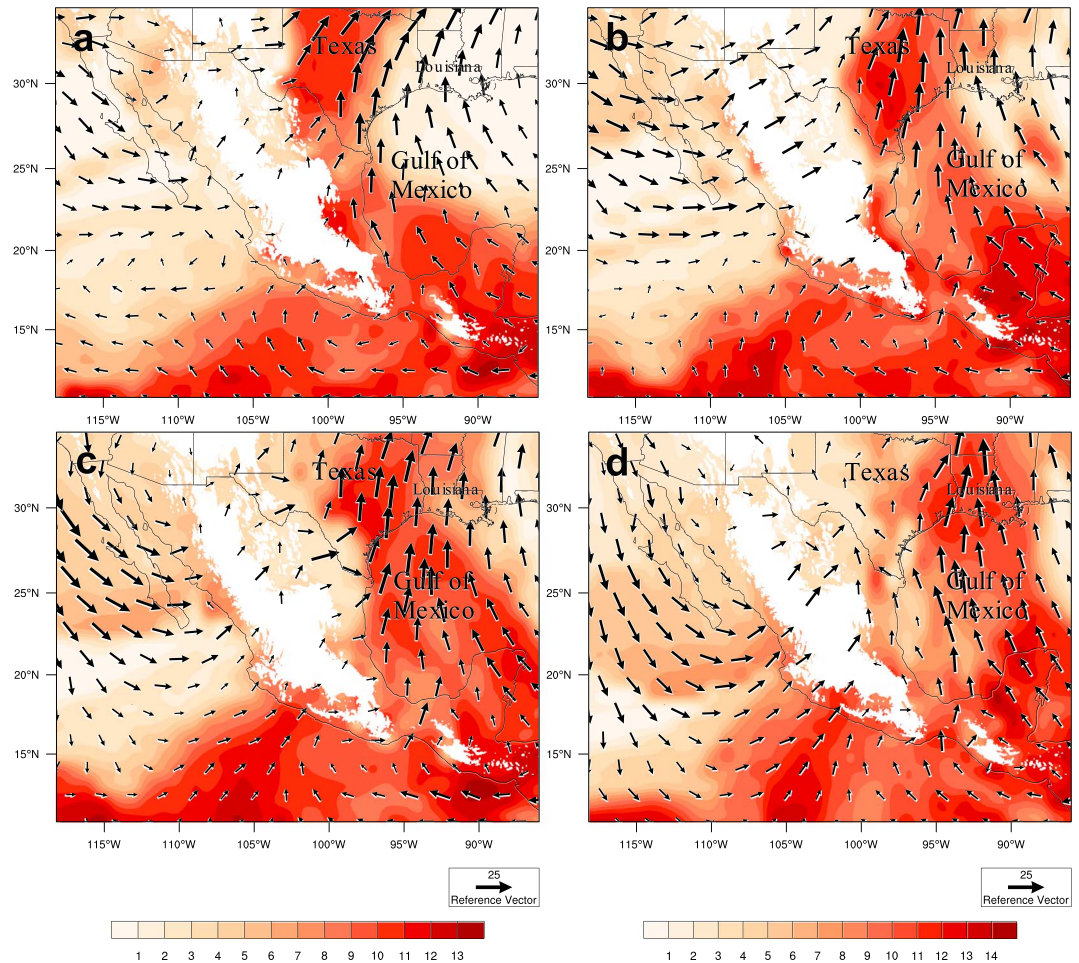


Figure 3. The same as in Figure 2, but for 850 hPa water vapor mixing ratio * 1000 (g/kg) and wind vector (m/s).

12 km ensembles provide ensemble BE for both 12 km and 4 km hybrid analysis. The static BEs are generated using the National Meteorological Center method with the past 1 month of differences between WRF 12 and 24 h daily forecasts, using GFS data as the initial and boundary conditions.

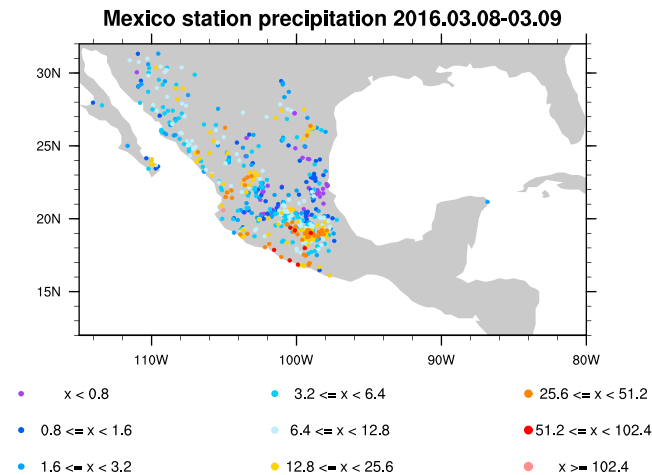


Figure 4. The Mexico station precipitation observation during 1400 UTC 8 March to 9 March.

Two parallel hybrid experiments were configured to evaluate the impact of assimilating GOES imager radiances for this heavy rainfall event over Mexico. All hybrid experiments produced separate, independent 12 km and 4 km analyses. At each analysis cycle, the background is modified with a blending scheme [Wang et al., 2014]. The first experiment (hereafter "CON") assimilated conventional observations from radiosondes, ships, Tropospheric Airborne Meteorological Data Reporting (TAMDAR), satellite-derived winds, land and oceanic surface stations in both outer and inner domains (Figure 6), and the advanced microwave sounding unit-A (AMSU-A) on NOAA-15, 16, 18,

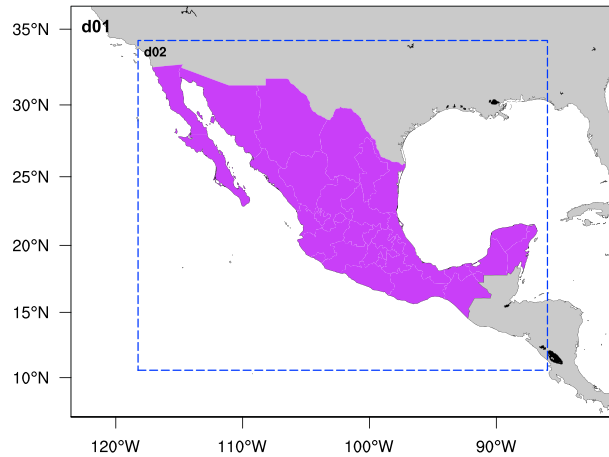


Figure 5. The experimental domains for d01 and d02.

and 19 in the outer domain. The second experiment (hereafter, "GOES_IMG") assimilated the same observations from CON plus clear-sky GOES imager radiances in both outer and inner domains. The GOES imager radiances were thinned to a 30 km grid in outer domain and 10 km grid in the inner domain, while the AMSU-A radiance data were thinned on a 120 km grid to avoid potential correlations [Liu and Rabier, 2002]. Channel 1 is the visible channel, which cannot be assimilated in the current assimilation system. The channel 2 data are affected by the solar radiation at day time and only used at nighttime. Infrared channel 2, 4, and

6's weighting function peaks are at low level. They are more sensitive to the surface emissivity, which has large uncertainty over land. So in GOES_IMG experiment, they were assimilated only over ocean, while water vapor channel 3 was used over both land and ocean.

5. Result

All results described in the following subsections are from 4 km inner domain.

5.1. Radiance Simulation in GOES_IMG

Since the water vapor channel is very useful for detecting both small and large-scale atmospheric features, we choose GOES-13 water vapor channel as an example. Figure 7 shows channel 3 observations (Figure 7a), the temperature and relative humidity cross section (Figure 7b) along AB line in Figure 7a, and simulated brightness temperature (Figure 7c) from background at 00 UTC 9 March. Because of the GOES-13's coverage, imager observations can cover the whole domain. With the corresponding weighting function, the water vapor channel radiance is correlated with the humidity on middle and upper troposphere. The brightness temperature images (Figures 7a and 7c) are pseudocolor images. The color bar on the bottom of the image extends from warm and dry on the right to cold and cloudy on the left. In this image, dry areas are dark, orange; brighter shades of gray depict increasingly moist areas, while cirrus clouds and thunderstorm tops are colored magenta, cyan, and green.

In Figure 7a, there is a clear warm conveyor belt extended from Mexico to the south United States with brighter shades and a dry conveyor belt over east Pacific Ocean with dark color. The dark dry regions are caused by descent, and light regions are by ascent, which in turn are associated with upper level convergence and divergence, respectively [Georgiev and Martin, 2001].

From Figure 7b, at the west side, the air is warmer and dryer associated with subsidence and advection processes. Above the Sierra Madre Occidental, the east part, colder air, and higher moisture values are found to produce lower radiance values and a brighter appearance in the image. Usually, the convective process occurs in the front of dry conveyor belt. Because CRTM clear-sky scheme was used in GOES_IMG, the simulated

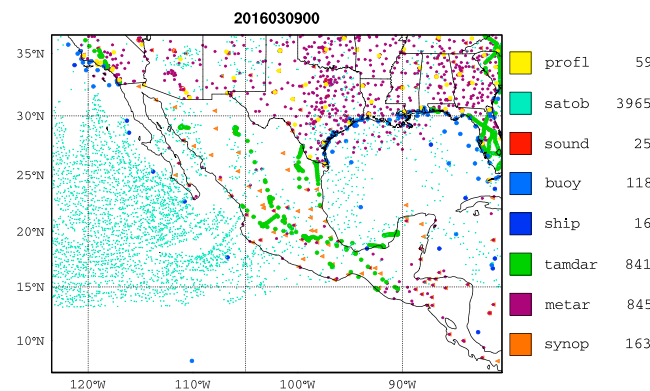


Figure 6. The distribution of observation used in the CON experiment at 00 UTC 9 March 2016. The numbers of each observation are marked on the right.

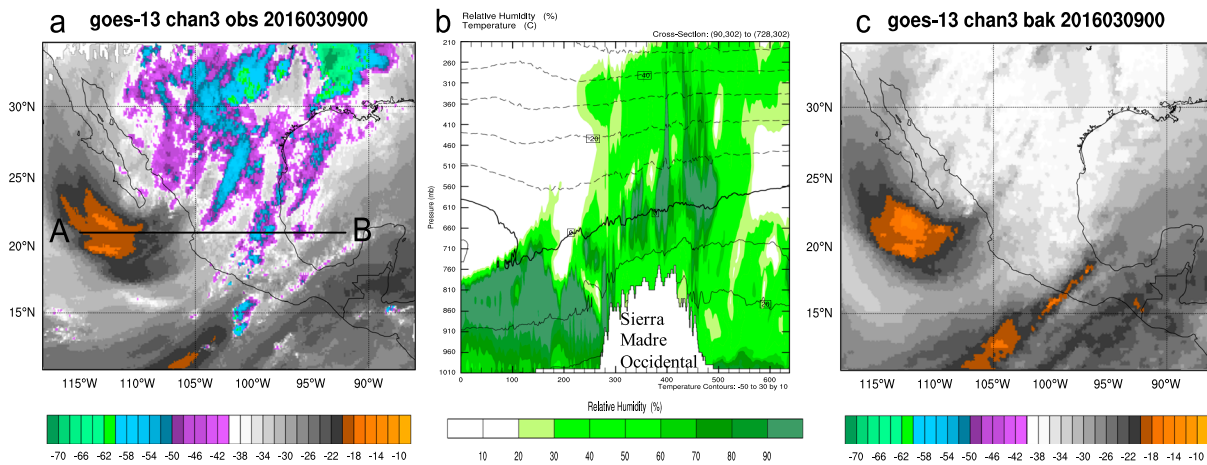


Figure 7. (a) GOES-13 imager channel 3 observation (°C), (b) the cross section of temperature (°C) and relative humidity (%) along AB line in Figure 7a, and (c) simulated brightness temperature from background at 0000 UTC 9 March.

observations (Figure 7c) are larger than observed values over the cloudy area. With the large difference, these observations will be rejected in the assimilation cycles.

After quality control, 17,104 water vapor channel observations are assimilated in GOES_IMG at 0000 UTC 9 March. From the scatterplot (Figure 8), the bias is reduced clearly after bias correction. That means that the bias correction scheme for GOES is effective. As shown in Figure 8c, GOES assimilation significantly improves the analysis quality with reducing the standard deviation and root-mean-square of OMA (observation minus analysis) from 1.318 to 0.495 and 1.388 to 0.495, respectively.

Furthermore, this improvement is consistent from the first cycle to the last one. From Figures 9a–9c, more than 15,000 observations are assimilated for all channels after quality control. The number of assimilated observations shows a 3 h oscillation. It is because full-disk observations are available at each 0000/0300/0600/0900/1200/1500/1800/2100 UTC, but partial coverage at other analysis times. Before bias correction, channel 3 has about 3 K positive bias, while channel 4 and channel 6 have -0.5 K bias. These biases are removed with variational bias correction. After GOES assimilation, channel 3 obtains the most visible reduction in the standard deviation. It indicates that GOES imager assimilation can improve the analysis quality consistently.

5.2. Impact on Analysis

Figure 10 shows the difference of 500 hPa height and 850 hPa water vapor mixing ratio between two experiments' analysis (GOES_IMG – CON). In the upper low area (Figure 10a), GOES_IMG generates a deeper low.

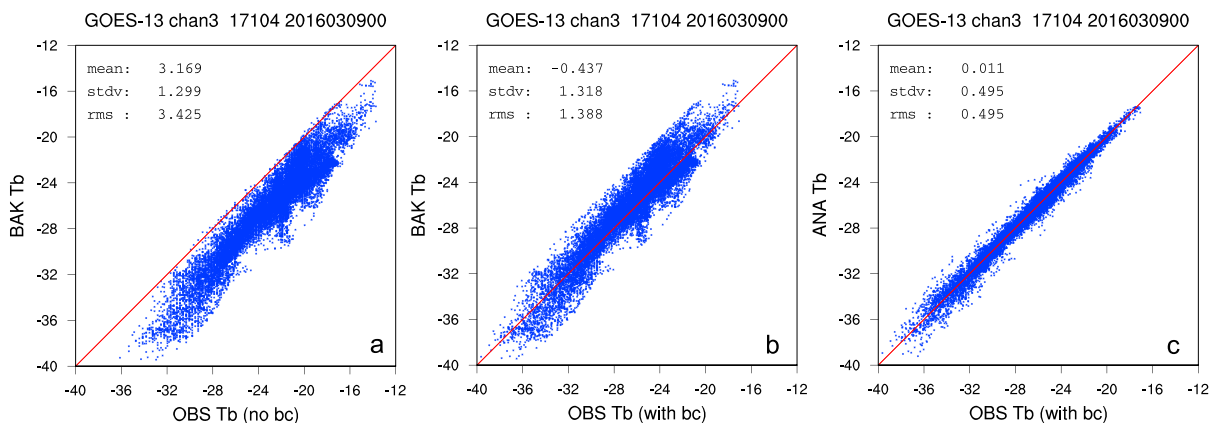


Figure 8. The scatterplot of observation versus CRTM-calculated brightness temperature (Tb, K) from background (a) before and (b) after bias correction and versus (c) CRTM-calculated brightness temperature from analysis valid at 00 UTC 9 March.

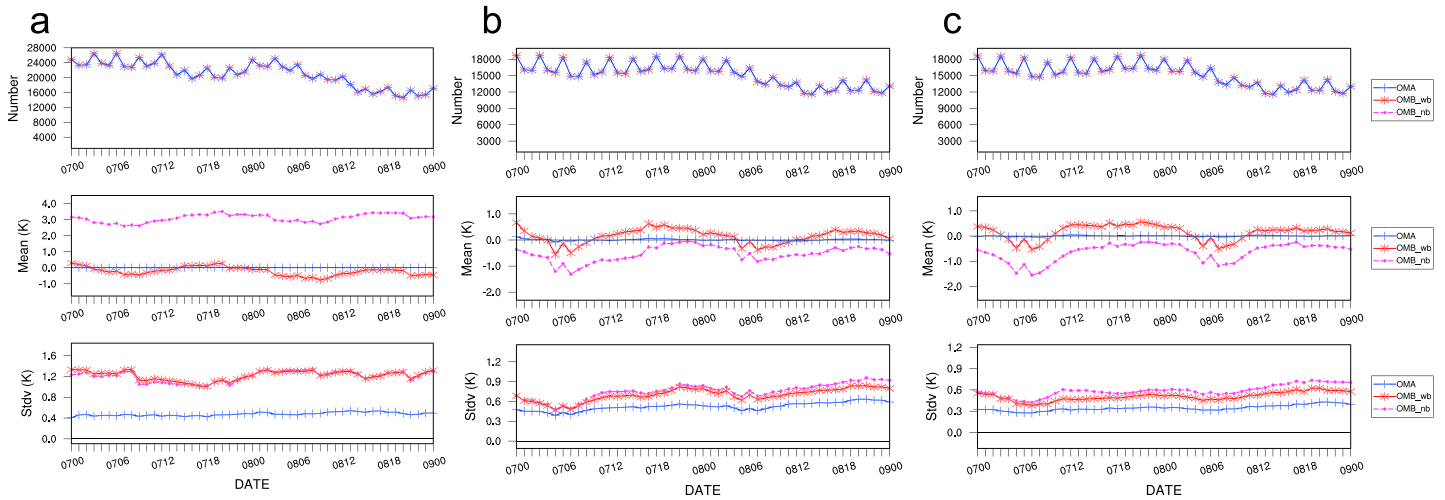


Figure 9. The observation number, mean bias, and standard deviation for (a) channel 3, (b) channel 4, and (c) channel 6 with OMB (observation minus background, pink), OMB with bias correction (red), and OMA (blue) valid from 00 UTC 7 March to 00 UTC 9 March 2016.

Behind the upper trough, GOES_IMG height is higher than CON, while lower in the front of trough. It means that after GOES assimilation, the system develops stronger and moves faster. In the lower level (Figure 10b), a clear moisture band occurs on the east Pacific Ocean. With the low-level wind, more water vapors are transported to the Mexico west coast.

With the hourly cycling configuration, the TAMDAR data, which have high temporal resolution, are selected to verify the analysis. The curve of TAMDAR observation number has a valley every day; it is because the period from 0800 UTC to 1100 UTC is the early morning of Mexico, no aircraft works. In Figure 11a, verified with the humidity Q of TAMDAR data, CON and GOES_IMG have the similar mean OMA and RMSE (root-mean-square error) at the beginning of assimilation experiment. After 24 cycles, GOES_IMG obtains smaller mean OMA and RMSE than CON. Similar to parameter Q , parameter temperature T from GOES_IMG (Figure 11b) also brings some improvement.

Besides the TAMDAR data, all-sky GOES imager observations are also selected to verify the analysis quantity. At 0000 UTC 9 March (Figure 12a), the upper low was developing and moving to the west coast of Mexico. Compared with the GOES imager observation, the simulated brightness temperatures from two experiments' analyses all depicted the main warm conveyor belt, dry conveyor belt, and the heavy cloudy area over

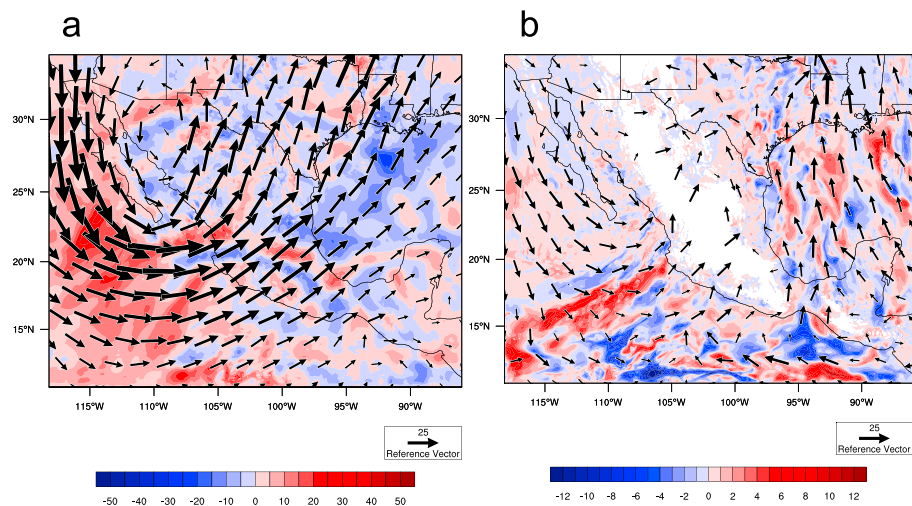


Figure 10. The difference of 500 hPa height (m) and 850 hPa water vapor mixing ratio (g/kg) between GOES_IMG and CON analysis at 0000 UTC 9 March. The wind vectors are from GOES_IMG.

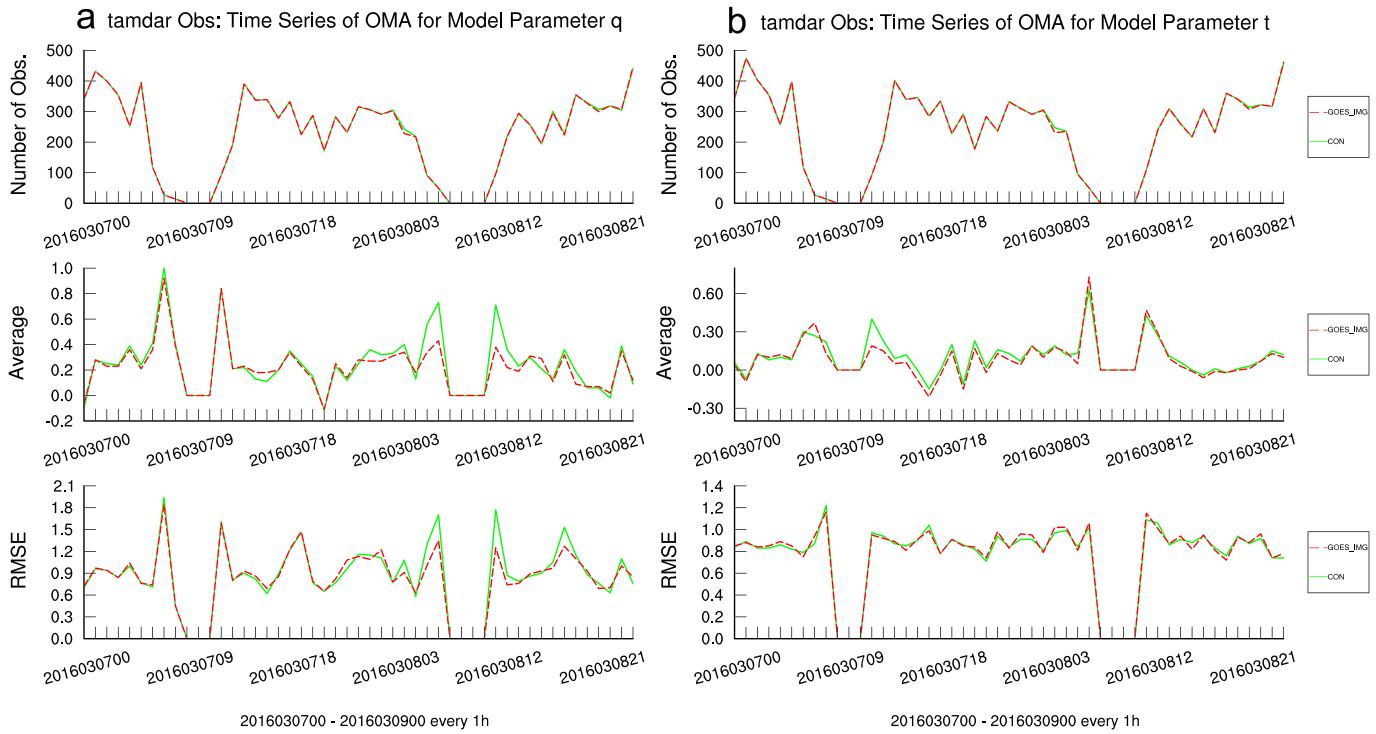


Figure 11. The time series of OMA for (a) specific humidity q (g/kg) and (b) temperature t (Kelvin) of CON (green) and GOES_IMG (red) from 0000 UTC 7 March to 0000 UTC 9 March.

Arkansas, United States. However, in Figure 12a, there are some separate northeast-southwest high cloud belts over the Mexico and the Gulf of Mexico. CON produced a whole cloudy area (Figure 12b), while GOES_IMG (Figure 12c) obtained more realistic cloud pattern and apparently agreed more closely with the GOES imager observation. Note that our clear-sky radiance assimilation will not affect cloud fields for a single analysis, but effects on cloud fields will be accumulated with time from cycling forecast-analysis procedure. Moreover, a nonexistent high water vapor area occurred at the south of CON analysis (Figure 12b). From the cross section of this area, relative humidity exceeded 90% between 750 hPa and 550 hPa in CON analysis (Figure 13a). At the upper troposphere, CON produced higher moisture values (>80%) than those from GOES_IMG (Figure 13b). Therefore, the simulated water vapor channel brightness temperature originating from that layer produced lower values (Figure 12b).

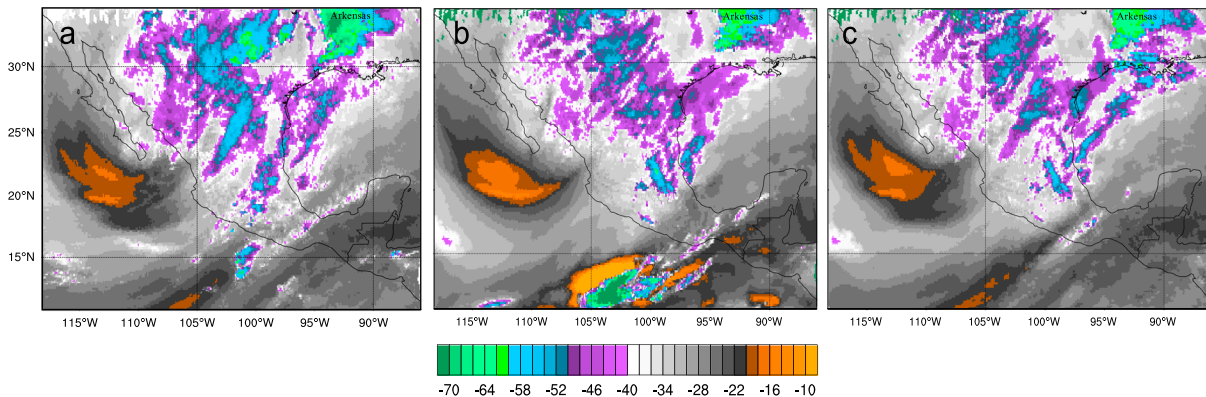


Figure 12. The cloudy simulated GOES-13 imager channel 3 brightness temperatures from the (a) GOES observation comparing with the analysis of (b) CON and (c) GOES_IMG at 0000 UTC 9 March.

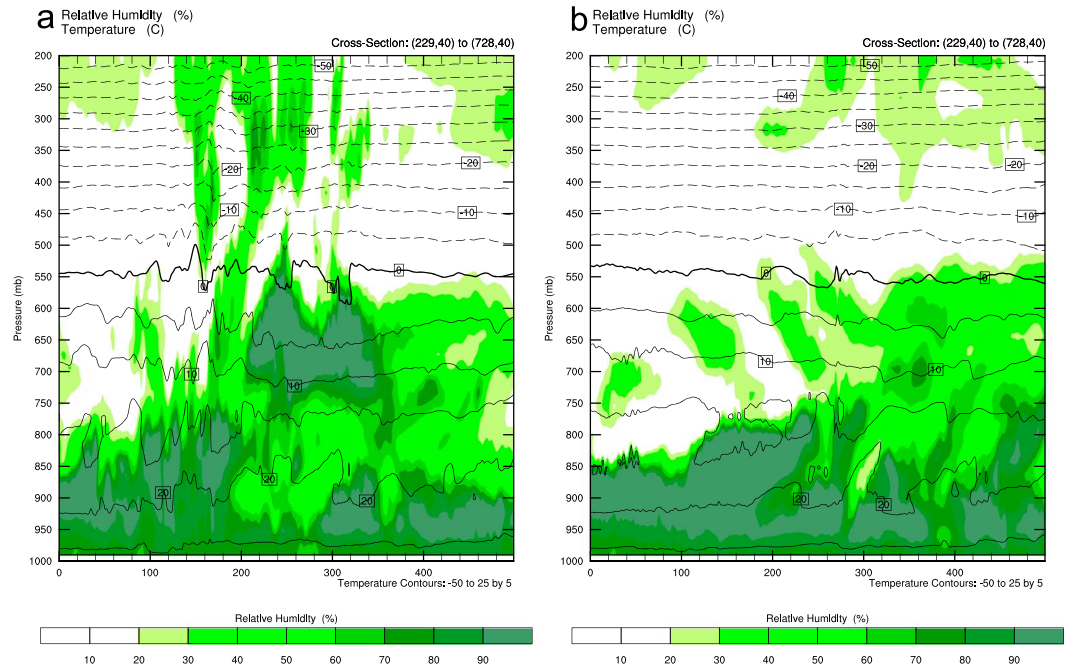


Figure 13. The cross section of temperature (°C) and relative humidity (%) from (a) CON and (b) GOES_IMG at 12°N from 92 to 110°W.

5.3. Impact on Forecast

Four 24 h forecasts, initialized from 1200 UTC 7 March to 0000 UTC 9 March every 12 h, were made to evaluate the impact of GOES imager assimilation on forecast. At forecast time, the TMADAR observations are distributed from surface to 200 hPa. As seen from Figure 14, the improvement from GOES imager radiance assimilation can be seen on the temperature field at low and upper levels. For humidity, the very minor forecast impact is demonstrated at middle troposphere. The wind forecast obtained the significant improvement around 850 hPa, but negative impact around 500–400 hPa, which is likely due to the limited TAMDAR wind observations.

At 0000 UTC 10 March, the 24 h forecast from 0000 UTC 9 March, the upper trough moved across the Mexico. The air current at the front of trough brought more water vapor to the west coast of Mexico from Pacific Ocean and to the south United States from the Gulf of Mexico, resulting in a heavy and high moisture area. Verified with GOES all-sky observation, the 24 h forecast of CON (Figure 15b) and GOES_IMG (Figure 15c) achieved the similar pattern, but the heavier and larger cloudy areas were further north. For CON forecast, the cloud was separated over the Gulf of Mexico, while GOES_IMG obtained the similar cloudy coverage as the GOES imager observations on the west coast of the Gulf of Mexico.

Figure 16 shows the time series of the observation number, which is used in the forecast verification, and the OMF (observation minus forecast) standard deviation of channels 3, 4, and 6 for CON and GOES_IMG from four 24 h forecasts. Because full-disk data are used every 3 h, the observation numbers at 0000/0300/0600/0900/1200/1500/1800/2100 UTC are larger than other times. In Figures 16b–16d, with the cloudy simulation, channel 3 has the smallest standard deviation than channel 4 and channel 6. The standard deviations of three channels increase with forecast range (particularly for the first 12 h), but GOES_IMG forecast gained a significant and consistent improvement for the whole forecast period. Channel 3 standard deviation reduced 25%, while 18% for channel 4 and 20% for channel 6.

5.4. Impact on Precipitation Forecast

In this case, the deep upper trough brought more water vapor from Pacific Ocean to the west coast of Mexico and produced torrential rain. The 24 h precipitation forecast, initialized at 1400 UTC 8 March, was verified with Mexico station precipitation data.

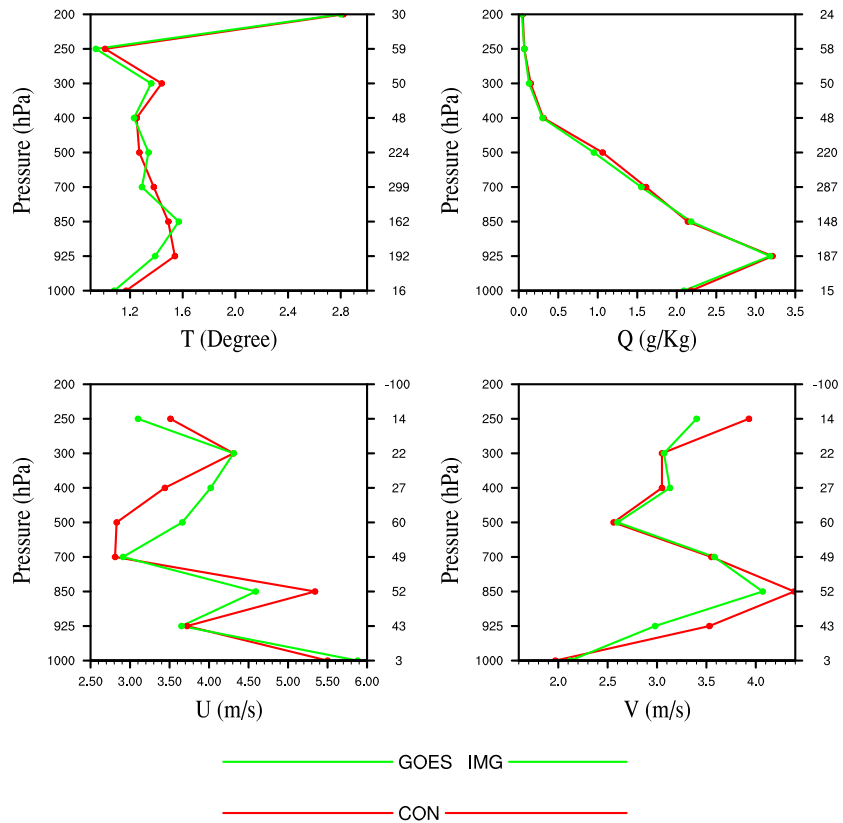


Figure 14. The RMSE profile of 4 12 h forecasts from CON (red line) and GOES_IMG (green line) verified with TAMDAR data.

Figure 17 displayed the 850 hPa and 300 hPa wind forecast difference from CON and GOES_IMG at 1400 UTC 9 March. The characteristic of convergence at the 850 hPa (Figure 17a) over heavy rainfall area can be seen clearly. At 300 hPa (Figure 17b), the wind field showed a divergence pattern over this area. The structure with wind convergence in low level and the divergence in upper level near rainfall location indicate the strengthening of the convection with GOES imager data assimilation. This is associated with intensified rainfall forecast in the GOES_IMG experiment, as shown in Figure 18.

The impact of GOES assimilation on precipitation forecast is quantitatively assessed with the fractions skill score (FSS) [Roberts, 2005; Schwartz et al., 2010], defined as

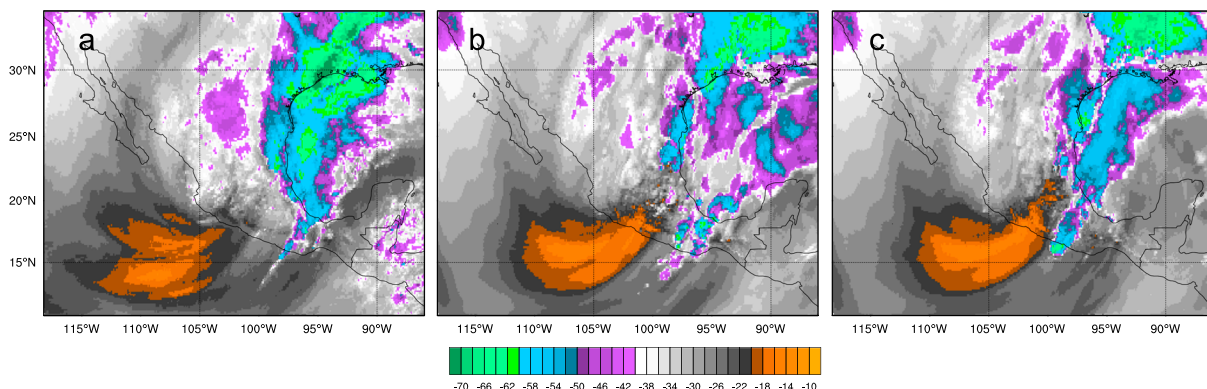


Figure 15. The same as in Figure 13, but from 24 h forecast valid at 0000 UTC 10 March of (a) GOES imager observation compared with (b) CON and (c) GOES_IMG.

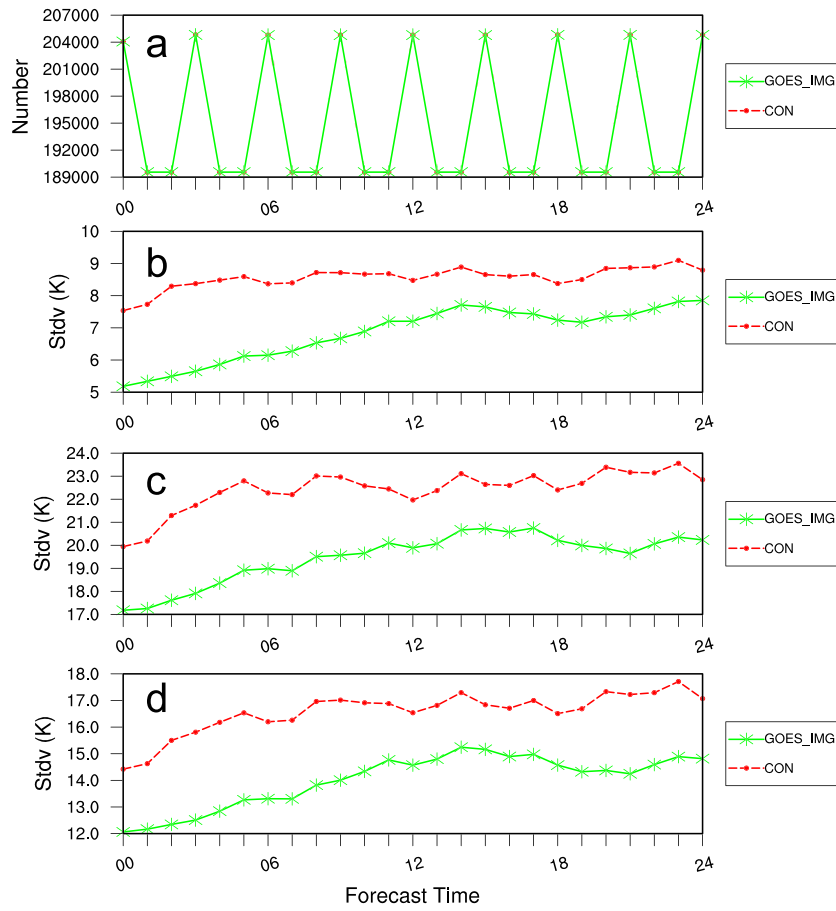


Figure 16. The time series of the (a) observation number and the OMF (observation minus forecast) standard deviation of channels (b) 3, (c) 4, and (d) 6 for CON (red) and GOES_IMG (green) from four 24 h forecasts.

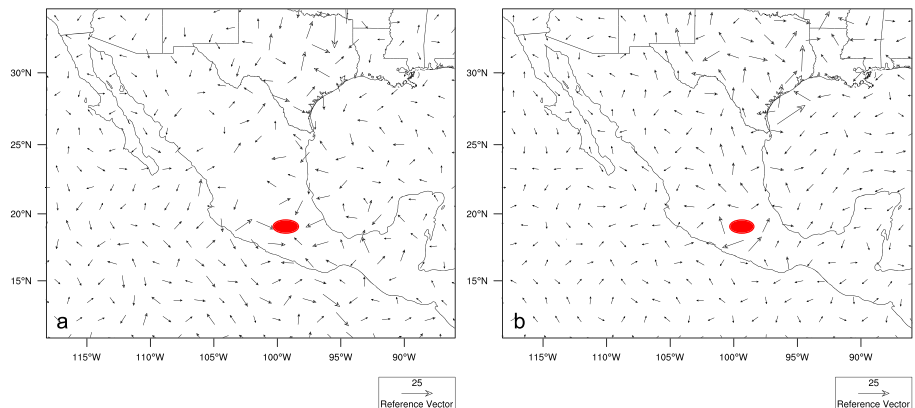


Figure 17. The difference of wind forecast between CON and GOES_IMG at 1400 UTC 9 March at (a) 850 hPa and (b) 300 hPa. The red area represents heavy rainfall area.

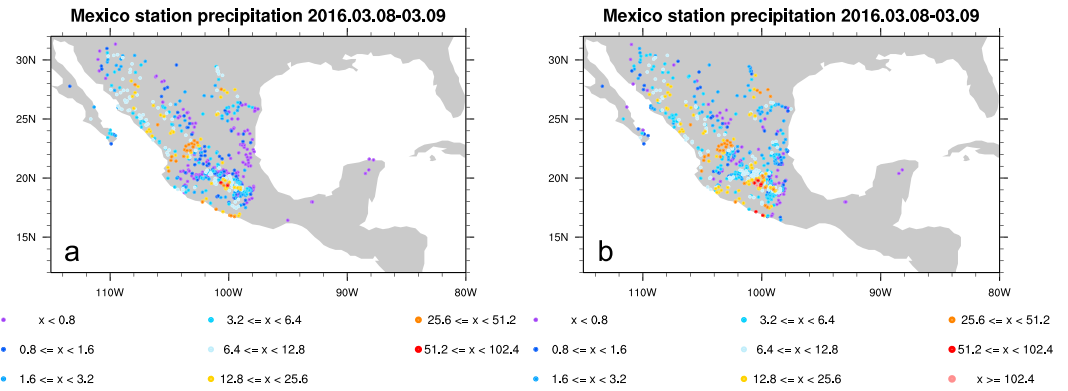


Figure 18. The 24 h accumulated precipitation map from 1400 UTC 8 March to 1400 UTC 9 March. (a) CON and (b) GOES_IMG.

$$FBS = \frac{1}{N_v} \sum_{i=1}^{N_v} [NP_{F(i)} - NP_{O(i)}], \quad (14)$$

$$FBS_{\text{worst}} = \frac{1}{N_v} \left[\sum_{i=1}^{N_v} NP_{F(i)}^2 + \sum_{i=1}^{N_v} NP_{O(i)}^2 \right], \quad (15)$$

$$FSS = 1 - \frac{FBS}{FBS_{\text{worst}}}. \quad (16)$$

FBS is Fractions Brier Score and $NP_{F(i)}$ and $NP_{O(i)}$ are the neighborhood probabilities at the i th grid box in the model forecast and observed fraction fields, respectively. N_v is the number of points within the verification domain on the verification grid. i ranges from 1 to N_v . The FSS ranges from 0 to 1. A score of 1 indicates perfect performance, and a score of 0 is attained for no skill.

The Bias is another skill score of precipitation, defined as

$$\text{Bias} = \frac{H + F}{H + O}, \quad (17)$$

where H represents the number of both forecast and the observations meet or exceed the threshold; F is the number of forecasts at observation points with precipitation equal to or exceed a given threshold; O is the number of occurrences in which the observations meet or exceed the threshold. The Bias indicates whether the forecast system has a tendency to underforecast ($\text{Bias} < 1$) or overforecast ($\text{Bias} > 1$). The perfect score is 1.

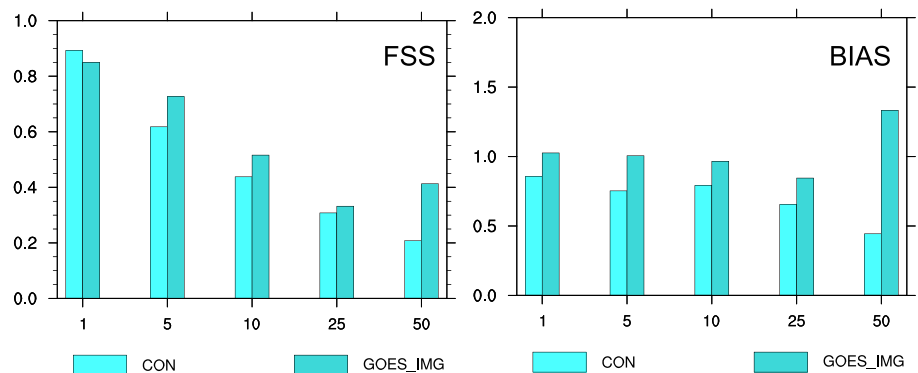


Figure 19. The FSS and Bias for 24 h accumulated precipitation (mm) from 1400 UTC 8 March to 1400 UTC 9 March. Radius of influence is 12 km (three grids).

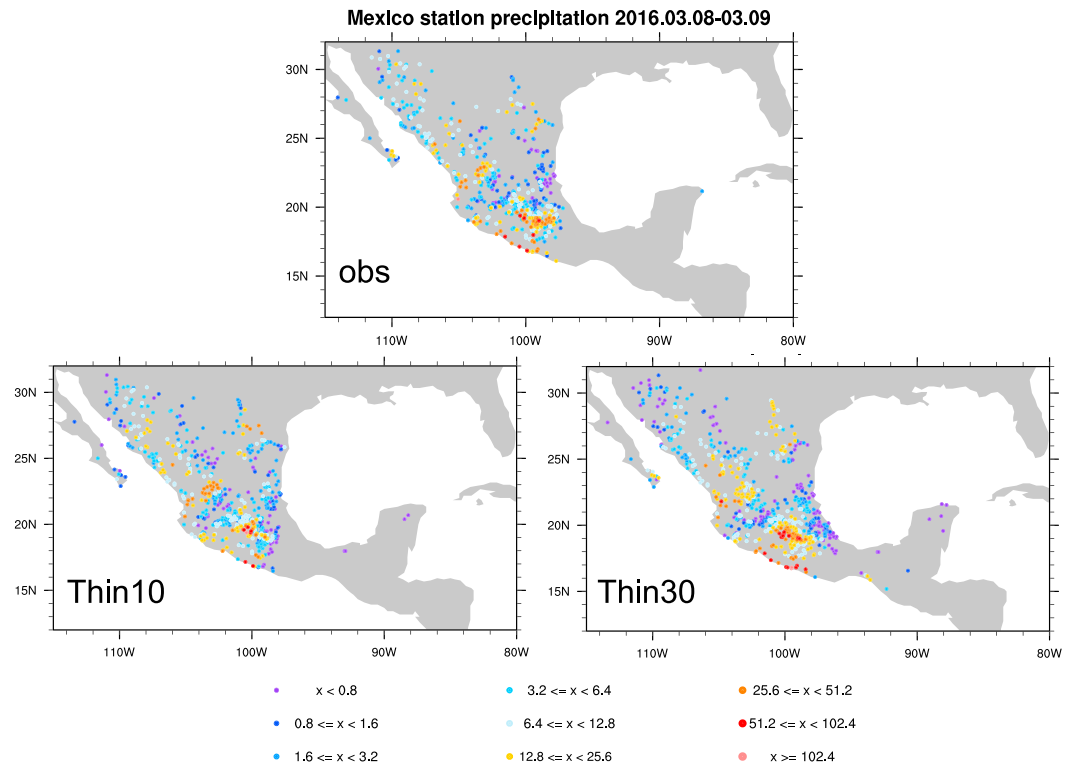


Figure 20. Same as in Figure 18, but (a) observed precipitation, (b) Thin10, and (c) Thin30.

The FSS and Bias for 24 h accumulated precipitation from 1400 UTC 8 March to 1400 UTC 9 March are displayed in Figure 19 for various precipitation thresholds. The radius of influence is 12 km (three grids). The FSS indicates that almost at all accumulation thresholds, the GOES_IMG produced more skillful forecasts than CON. Especially for extreme event prediction over 50 mm, GOES_IMG has an FSS score 0.4, while CON is only 0.2. For the Bias, CON has a tendency to underpredict at all rainfall thresholds, especially for extreme rainfall event. GOES_IMG has nearly a perfect Bias score from 1 mm to 10 mm rainfall but overpredicted at 50 mm. This finding indicates that the GOES_IMG substantially improves precipitation forecast.

5.5. Sensitivity to Thinning Mesh

Based on GOES imager’s high resolution, 10 km was selected as the thinning mesh for inner domain in GOES_IMG (renamed as “Thin10”). An additional experiment (denote as “Thin30”) was conducted to see the sensitivity to thinning mesh. The assimilation configuration was the same as Thin10, except for 60 km

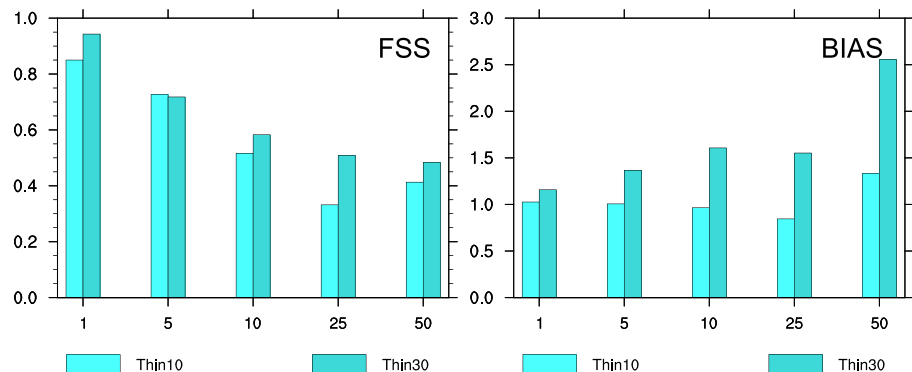


Figure 21. Same as in Figure 19, but for Thin10 and Thin30.

thinning mesh for outer domain and 30 km thinning mesh for inner domain. A 24 h precipitation forecast was made from 1400 UTC 8 March to 1400 UTC 9 March. The 24 h accumulated rainfall map and precipitation scores are shown in Figure 20c and Figure 21.

Compared with Thin10 24 h accumulated precipitation map (Figure 20b), Thin30 obtains heavier rainfall on the west-south coast of Mexico, which is closer to the station observations (Figure 20a). Around central Mexico, Thin30 intensifies the precipitation and expands the rainfall center eastward, which is also larger than the observed one. Because more stations produce rainfall, Thin30 forecast gains better FSS than Thin10. However, since many station precipitations in Thin30 forecast are heavier than observation, the BIAS of Thin30 for all thresholds indicates a significant overprediction, which is consistent with Figure 20. It should be pointed out that ideal thinning mesh should be adaptive according to weather situation, e.g., using more observations around locations with larger gradient. The result from current uniform thinning mesh may vary case by case. The reader should use conclusion obtained here with caution.

6. Conclusion

This study is the first attempt to assimilate GOES imager radiance data using rapid refresh system with hybrid-3D-EnVar scheme and to evaluate its impact for convective process over Mexico in 7–10 March 2016 with a convection-permitting model setting (4 km grid spacing). The GOES imager observations used in this study are GVAR data in NetCDF format. The calibration and satellite zenith angle calculation were implemented within WRFDA. The hourly forecast-analysis cycling experiments were conducted using WRF and WRFDA hybrid to evaluate the impact of assimilating clear-sky GOES imager radiances, comparing to a benchmark experiment without the assimilation of GOES imager radiances.

With the GOES imager radiance assimilation, the upper trough moved fast and more water vapor was transported to the west coast of Mexico. Compared with CON, GOES_IMG improved humidity and temperature analysis and obtained more similar water vapor channel image to the observations, while there was a false cloudy area from CON analysis. Significant and consistent standard deviation reductions from the 24 h forecast were produced for all assimilated channels verified with GOES all-sky observations. Verifying against the station precipitation observation, significant positive forecast impact from assimilating GOES imager radiances was achieved. Furthermore, enlarging the thinning mesh improved the FSS but caused overprediction.

Further improvements could be made for GOES imager assimilation in the future. For example, the all-sky radiance assimilation [e.g., Yang *et al.*, 2016] can assimilate more observations under cloudy and precipitating areas to provide more accurate convective structure information. In addition, other advanced assimilation methods such as 4D-Var and hybrid-4D-EnVar could be more effective in extracting information content in a more frequent basis (e.g., every 15 min for GOES imager).

Acknowledgments

The first author was jointly supported by the National Basic Research Program of China (2013CB430102), the National Natural Science Foundation of China (41430427), the Key University Science Research Project of Jiangsu Province (11KJA170001), and the Priority Academic Program Development of Jiangsu Higher Education Institutions (PAPD). We are also grateful to the Panasonic Avionics Corporation for funding this work. NCAR is sponsored by the National Science Foundation. The GOES imager data used in this study were obtained freely from the Comprehensive Large Array-Data Stewardship System of NOAA (https://www.class.ngdc.noaa.gov/saa/products/search?datatype_family=GVAR_IMG) following registration.

References

- Auligné, T., A. P. McNally, and D. P. Dee (2007), Adaptive bias correction for satellite data in a numerical weather prediction system, *Q. J. R. Meteorol. Soc.*, *133*, 631–642.
- Barker, D. M., et al. (2012), The Weather Research and Forecasting (WRF) model's community variational/ensemble data assimilation system: WRFDA, *Bull. Am. Meteorol. Soc.*, *93*, 831–843.
- Bauer, P., A. J. Geer, P. Lopez, and D. Salmond (2010), Direct 4DVar assimilation of all-sky radiances. Part I: Implementation, *Q. J. R. Meteorol. Soc.*, *136*, 1868–1885.
- Chen, F., and J. Dudhia (2001), Coupling an advanced land-surface/hydrology model with the Penn State/NCAR MM5 modeling system. Part I: Model description and implementation, *Mon. Weather Rev.*, *129*, 569–585.
- Chen, Y., H. Wang, J. Min, X. Huang, P. Minnis, R. Zhang, J. Haggerty, and R. Palikouda (2015), Variational assimilation of cloud liquid/ice water path and its impact on NWP, *J. Appl. Meteor. Climatol.*, *54*(8), 1809–1825.
- Chen, Y., R. Zhang, D. Meng, J. Min, L. Zhang (2016), Variational Assimilation of Satellite Cloud Water/Ice Path and Microphysical Scheme Sensitivity to the Assimilation of A Rainfall Case, *Adv. Atmos. Sci.*, *33*(10), 1158–1170.
- Dee, D. P. (2004), Variational bias correction of radiance data in the ECMWF system. In: Proc. of the ECMWF Workshop on Assimilation of High Spectral Resolution Sounders in NWP, Reading, U. K., 28 June–1 July.
- Geer, A. J. and P. Bauer (2010), Enhanced use of all-sky microwave observations sensitive to water vapor, Cloud and Precipitation, Tech. Memo. ECMWF, vol. 620, 41 pp., Reading, U. K.
- Geer, A. J., P. Bauer, and P. Lopez (2010), Direct 4D-Var assimilation of all-sky radiances. Part II: Assessment, *Q. J. R. Meteorol. Soc.*, *136*, 1886–1905.
- Georgiev, C., and F. Martin (2001), Use of potential vorticity fields, Meteosat water vapour imagery and pseudo water vapour images for evaluating numerical model behavior, *Meteorol. Appl.*, *8*, 57–69.
- Greenwald, T. J., R. Hertenstein, and T. Vukicevic (2002), An all weather observational operator for radiance data assimilation with mesoscale forecast models, *Mon. Weather Rev.*, *130*, 1882–1897.

- Guidard, V., N. Fourrié, P. Brousseau, and F. Rabier (2011), Impact of IASI assimilation at global and convective scales and challenges for the assimilation of cloudy scenes, *Q. J. R. Meteorol. Soc.*, *137*, 1975–1987.
- Heilliette, S. (2010), Assimilation of cloud-affected infrared radiances at environment Canada. ECMWF-JCSDA Workshop, 15-17 June 2010, Reading, U. K.
- Heilliette, S., and L. Garand (2007), A practical approach for the assimilation of cloudy infrared radiances and its evaluation using AIRS simulated observations, *Atmos. Ocean*, *45*, 211–225.
- Hocking, J., P. Francis, and R. Saunders (2010), Cloud detection in Meteosat second generation imagery at the Met Office, Forecasting R&D Tech. Rep. 540.
- Hong, S., Y. Noh, and J. Dudhia (2006), A new vertical diffusion package with an explicit treatment of entrainment processes, *Mon. Weather Rev.*, *134*, 2318–2341.
- Iacono, M. J., J. S. Delamere, E. J. Mlawer, M. W. Shephard, S. A. Clough, and W. D. Collins (2008), Radiative forcing by longlived greenhouse gases: Calculations with the AER radiative transfer models, *J. Geophys. Res.*, *113*, D13103, doi:10.1029/2008JD009944.
- Kain, J. S. (2004), The Kain-Fritsch convective parameterization: An update, *J. Appl. Meteorol.*, *43*, 170–181.
- Kazumori, M. (2014), Satellite radiance assimilation in the JMA operational mesoscale 4DVAR system, *Mon. Weather Rev.*, *142*, 1361–1381.
- Köpken, C., G. Kelly, and J.-N. Thépaut (2004), Assimilation of Meteosat radiances data within the 4D-Var system at ECMWF: Assimilation experiments and forecast impact, *Q. J. R. Meteorol. Soc.*, *130*, 2277–2292.
- Liu, Z., and F. Rabier (2002), The interaction between model resolution, observation resolution and observation density in data assimilation: A one-dimensional study, *Q. J. R. Meteorol. Soc.*, *128*, 1367–1386.
- Liu, Z., C. S. Schwartz, C. Snyder, and S. Ha (2012), Impact of assimilation AMSU-A radiances on forecast of 2008 Atlantic tropical cyclones initialized with a limited-area ensemble Kalman filter, *Mon. Weather Rev.*, *140*, 4017–4034.
- Lorenc, A. C. (2003), The potential of the ensemble Kalman filter for NWP-A comparison with 4D-VAR, *Q. J. R. Meteorol. Soc.*, *129*, 3183–3203.
- Lupu, C. and A. P. McNally (2012), Assimilation of cloud-affected radiances from Meteosat-9 at ECMWF. EUMETSAT/ECMWF Fellowship Programme research reports, No. 25, ECMWF, 33 pp., Reading, U. K.
- McNally, A. P. (2009), The direct assimilation of cloud-affected satellite infrared radiances in the ECMWF 4D-Var, *Q. J. R. Meteorol. Soc.*, *129*, 2411–2323.
- McNally, A. P., P. D. Watts, J. A. Smith, R. Engelen, G. A. Kelly, J.-N. Thépaut, and M. Matricardi (2006), The assimilation of AIRS radiance data at ECMWF, *Q. J. R. Meteorol. Soc.*, *132*, 935–957.
- Mlawer, E. J., S. J. Taubman, P. D. Brown, M. J. Iacono, and S. A. Clough (1997), Radiative transfer for inhomogeneous atmosphere: rRTM, a validated correlated-k model for the long-wave, *J. Geophys. Res.*, *102*, 16,663–16,682, doi:10.1029/97JD00237.
- Monin, A. S., and A. M. Obukhov (1954), Basic laws of turbulent mixing in the surface layer of the atmosphere [in Russian], *Contrib. Geophys. Inst. Acad. Sci. USSR*, *24*, 163–187.
- Montmerle, T., F. Rabier, and C. Fischer (2007), Relative impact of polar-orbiting and geostationary satellite radiances in the Aladin/France numerical weather prediction system, *Q. J. R. Meteorol. Soc.*, *133*, 655–671.
- Morrison, H., G. Thompson, and V. Tatarskii (2009), Impact of cloud microphysics on the development of trailing stratiform precipitation in a simulated squall line: Comparison of one- and two-moment schemes, *Mon. Weather Rev.*, *137*, 991–1007.
- Okamoto, K. (2013), Assimilation of overcast cloudy infrared radiances of the geostationary MTSAT-1R imager, *Q. J. R. Meteorol. Soc.*, *139*, 715–730.
- Pavelin, E. G., S. J. English, and J. R. Eyre (2008), The assimilation of cloud-affected infrared satellite radiances for numerical weather prediction, *Q. J. R. Meteorol. Soc.*, *134*, 737–749.
- Pangaud, T., N. Fourrié, V. Guidard, M. Dahoui, and F. Rabier (2009), Assimilation of AIRS radiances affected by mid- to low level clouds, *Mon. Weather Rev.*, *137*, 4276–4292.
- Qin, Z., X. Zou, and F. Weng (2013), Evaluating added benefits of assimilating GOES imager radiance data in GSI for coastal QPFs, *Mon. Weather Rev.*, *141*, 75–92.
- Roberts, N. M. (2005), An investigation of the ability of a storm scale configuration of the Met Office NWP model to predict flood-producing rainfall. Met Office Tech. Rep. 455, 80 pp.
- Schwartz, C. S., and Z. Liu (2014), Convection-permitting forecasts initialized with continuously cycling limited-area 3DVAR, ensemble Kalman filter, and “hybrid” variational-ensemble data assimilation systems, *Mon. Weather Rev.*, *142*, 716–738.
- Schwartz, C. S., Z. Liu, and X. Huang (2015), Sensitivity of limited-area hybrid variational-ensemble analyses and forecasts to ensemble perturbation resolution, *Mon. Weather Rev.*, *143*, 3454–3477.
- Schwartz, C. S., J. S. Kain, S. J. Weiss, M. Xue, D. R. Bright, F. Kong, K. W. Thomas, J. J. Levit, M. C. Coniglio, and M. S. Wandishin (2010), Toward improved convection-allowing ensembles: Model physics sensitivities and optimizing probabilistic guidance with small ensemble membership, *Weather Forecasting*, *25*, 263–280.
- Skamarock, W. C., et al. (2008), A description of the Advanced Research WRF version 3. NCAR Tech. Note NCAR/TN-475_STR, 133 pp.
- Stengel, M., et al. (2009), Assimilation of SEVIRI infrared radiances with HIRLAM 4D-Var, *Q. J. R. Meteorol. Soc.*, *135*, 2100–2109.
- Su, X., J. Derber, J. Jung, Y. Tahara, D. Keyse, and R. Treadon (2003), The usage of GOES imager clear-sky radiance in NCEP Global Data Assimilation System, in *Proceedings of the 12th Conference on Satellite Meteorology and Oceanography*, *Am. Meteorol. Soc.*, pp. 3.20, Long Beach, Calif.
- Szyndel, M. D. E., G. Kelly, and J.-N. Thépaut (2005), Evaluation of potential benefit of assimilation of SEVIRI water vapour radiance data from Meteosat-8 into global numerical weather prediction analyses, *Atmos. Sci. Lett.*, *6*, 105–111.
- Wang, H., X. Hang, D. Xu, and J. Liu (2014), A scale-dependent blending scheme for WRFDA: Impact on regional weather forecasting, *Geosci. Model Dev.*, *7*, 1819–1828.
- Wang, X., D. M. Barker, C. Snyder, and T. Hamill (2008a), A hybrid ETKF-3DVAR data assimilation scheme for the WRF model. Part I: Observing system simulation experiment, *Mon. Weather Rev.*, *136*, 5116–5131.
- Wang, X., D. M. Barker, C. Snyder, and T. Hamill (2008b), A hybrid ETKF-3DVAR data assimilation scheme for the WRF model. Part II: Real observation experiments, *Mon. Weather Rev.*, *132*, 1190–1200.
- Wang, X., D. F. Parrish, D. T. Kleist, and J. S. Whitaker (2013), GSI 3DVAR-based ensemble-variational hybrid data assimilation for NCEP Global Forecast System: Single-resolution experiments, *Mon. Weather Rev.*, *141*, 4098–4117.
- Weinreb, M. and D. Han (2011), Conversion of GVAR infrared data to scene radiance or temperature. [Available at: <http://www.ospo.noaa.gov/Operations/GOES/calibration/gvar-conversion.html>]
- Weng, F. (2007), Advances in radiative transfer modeling in support of satellite data assimilation, *J. Atmos. Sci.*, *64*, 3799–3807.
- Xu, D., X. Huang, H. Wang, A. P. Mizzi, and J. Min (2015), Impact of assimilation radiances with the WRFDA ETKF/3DVAR hybrid system on prediction of two typhoons in 2012, *J. Meteorol. Res.*, *29*, 28–40.

- Xu, D., Z. Liu, X. Huang, J. Min, and H. Wang (2013), Impact of assimilation IASI radiance observations on forecasts of two tropical cyclones, *Meteorol. Atmos. Phys.*, *122*, 1–18.
- Yang, C., Z. Liu, J. Bresch, S. R. H. Rizvi, X. Huang, and J. Min (2016), AMSR2 all-sky radiance assimilation and its impact on the analysis and forecast of Hurricane Sandy with a limited-area data assimilation system, *Tellus A*, *68*, 30,917.
- Zhu, Y., et al. (2013), Enhanced radiance bias correction in the National Centers for Environmental Prediction's Gridpoint Statistical Interpolation data assimilation system, *Q. J. R. Meteorol. Soc.*, *140*, 1479–1492.
- Zou, X., Z. Qin, and F. Weng (2011), Improved coastal precipitation forecasts with direct assimilation of GOES-11/12 imager radiances, *Mon. Weather Rev.*, *139*, 3711–3729.
- Zou, X., Z. Qin, and Y. Zheng (2015), Improved tropical storm forecasts with GOES-13/15 imager radiances assimilation and asymmetric vortex initialization in HWRF, *Mon. Weather Rev.*, doi:10.1175/MWR-D-14-00223.1.